JOURNAL OF GEOPHYSICAL RESEARCH, VOL. 107, NO. A12, 1454, doi:10.1029/2002JA009307, 2002

IMAGE/high-energy energetic neutral atom: Global energetic neutral atom imaging of the plasma sheet and ring current during substorms

P. C:son Brandt, R. Demajistre, E. C. Roelof, S. Ohtani, and D. G. Mitchell
Applied Physics Laboratory, Johns Hopkins University, Laurel, Maryland, USA

S. Mende
Space Science Laboratory, Berkeley, California, USA

Received 4 February 2002; revised 20 May 2002; accepted 19 July 2002; published 18 December 2002.

[1] Energetic neutral atom (ENA) images in the 10–60 keV range show the substorm dynamics of the ion distribution out to 14 R_E in the plasma sheet. The images were obtained during two substorms in the mainphase of the 4 October 2000 storm by the high-energy energetic neutral atom (HENA) imager on board the IMAGE satellite. During the two substorm sequences the edge of the most tailward ENA emissions appears to move earthward in association with dipolarization observed at geosynchronous distance by the GOES satellite. At the time of geosynchronous dipolarization, the auroral onset was observed by the far ultra violet (FUV) imager onboard IMAGE. Preliminary equatorial ion distributions derived from the individual ENA images in the substorm sequences have been obtained through a constrained linear inversion technique. The results show that the ion fluxes in the >8 R_E plasma sheet suddenly decrease around dipolarization during approximately 30 min. About 12–20 min after the start of the plasma sheet flux decrease, ion injections are seen by the geosynchronous satellites. The peak of the ring current flux is pushed in from geosynchronous to L = 4 over the substorm sequences. Two exospheric models are used in the inversion. We find that more realistic plasma sheet fluxes are obtained with an exospheric model that contains enhanced exospheric hydrogen densities on the nightside. Implications for earthward propagation of the plasma sheet ion distribution during dipolarization are discussed. *INDEX TERMS:* 2794 Magnetospheric Physics: Instruments and techniques; 2730 Magnetospheric Physics: Magnetosphere—inner; 2778 Magnetospheric Physics: Ring current; 2764 Magnetospheric Physics: Plasma sheet; *KEYWORDS:* ENA imaging, ring current, substorm, storm, plasma sheet

Citation: C:son Brandt, P., R. Demajistre, E. C. Roelof, S. Ohtani, D. G. Mitchell, and S. Mende, IMAGE/high-energy energetic neutral atom: Global energetic neutral atom imaging of the plasma sheet and ring current during substorms, *J. Geophys. Res.*, *107*(A12), 1454, doi:10.1029/2002JA009307, 2002.

1. Introduction

[2] The magnetospheric substorm is still the least understood global magnetospheric phenomena. One of the challenges has been to draw conclusions about the large-scale dynamics from local measurements in the geomagnetic tail and plasma sheet. Many substorm models have been developed, but two main models have emerged. The tail current disruption (TCD) model [*Lui*, 1991] and the near-Earth neutral line (NENL) model [*Baker et al.*, 1996]. Just before the onset of a substorm - the growth phase - magnetic flux from the lobes builds up in the plasma sheet and the x-component of the geomagnetic field increases. This is often the result of an increasing interplanetary electric field and results in increased cross tail current and thinning of the plasma sheet down to <1000 km in some cases. Prior to substorm onset, some observations [*Slavin et al.*, 2002] have been made that implies that reconnection of lobe flux takes place in the NENL region (x $\sim$ -22 to -30 R_E) resulting in high-speed earthward bulk flows ($\sim$100–1000 km/s). At substorm onset the cross-tail current disrupts in the $\sim$10–15 R_E region in the tail and an associated dipolarization of the geomagnetic field is observed [*Ohtani et al.*, 1992]. Immediately after dipolarization, proton injections are observed at geosynchronous altitude and below [*Reeves et al.*, 1996]. The NENL model [*Slavin et al.*, 2002] claims that it is the braking of the earthward flow of plasma as it reaches the inner magnetosphere, that triggers the TCD and dipolarization. On the other hand, the TCD model [*Lui*, 1991] claims that the increasing cross tail current triggers some instability that disrupts it and the subsequent dipolarization propagates both earthward and tailward from its onset location. In turn, this "rarefaction" wave would cause

0148-0227/02/2002JA009307$09.00

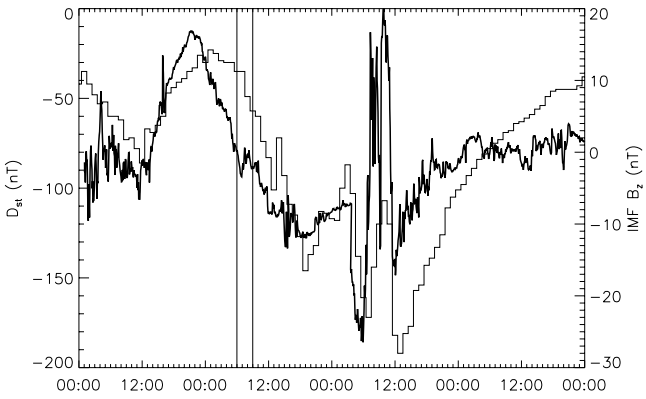

Figure 1. The IMF B_z (bold line) and the D_{st} (thin line) for the 4 October 2000 storm. The two vertical lines mark the time for the two substorms.

the reconnection observed in the NENL region. This debate motivated *Ohtani* [2001] to address a combined scenario where the reconnection at the NENL sets up a sufficient, but not necessary, condition for the triggering of the TCD.

[3] This paper reports the first global images of the energetic ion distributions in the near-Earth plasma sheet out to 14 R_E during two substorms in the mainphase of the 4 October 2000 storm. The images were obtained in the 10–60 keV range with 6 min resolution by the high-energy neutral atom (HENA) imager [*Mitchell et al.*, 2000] onboard the IMAGE satellite [*Burch*, 2000].

[4] [*Huang and Frank*, 1994] have summarized some average properties of the central plasma sheet at x ~ -10 to -25 R_E. They found that for an auroral electrojet (AE) index increasing from 0 to 1000 nT, the most dramatic change of the plasma was the ion temperature that changed from 3 to 7 keV. For the same activity levels the plasma bulk velocity $\left(\sqrt{\langle v_x\rangle^2 + \langle v_z\rangle^2 + \langle v_z\rangle^2}\right)$ was found to remain below 100 km/s and the ion distribution was relatively isotropic. The peak of the energy densities in the CPS are known to be located in the 2–50 keV range [*Kistler et al.*, 1992].

[5] Energetic neutral atoms (ENA) are produced when singly positively charged energetic ions undergo charge-exchange collisions with cold neutral atoms or molecules. The ions become neutral and propagate unaffected by electromagnetic fields. If the initial energy is much greater than the planetary escape energy (0.6 eV/nucleon), then the ENAs are unaffected by gravitational fields and will maintain their energy and momentum. In the terrestrial magnetosphere, the energetic ions will charge exchange with the geocorona at high altitudes and emit ENAs. In this way the ring current and the plasma sheet can be imaged. In addition to carrying with it spectral and directional information of the energetic ions, the ENAs also carries with them the compositional information of the ion distribution.

[6] The NENL is believed to form 22–30 R_E down the tail, whereas the onset of the TCD have been located outside geosynchronous. Tailward expansion of the onset region of TCD has been observed inside 15 R_E [*Ohtani et al.*, 1992], but it has been difficult to estimate the extent of the TCD onset region due to the sparse in-situ data available in this region. With present instrumentation, global ENA imaging can address phenomena that occurs inside 15 R_E. A natural question for ENA imaging of the plasma sheet is therefore what the extent of the TCD onset region is. However, we do not probe this problem in any detail in this paper.

[7] The purpose of this paper is to report the first global images of the dynamics of the plasma sheet and to present preliminary results and address some important issues of our inversions of the ENA images. The paper first describes the solar wind and geomagnetic conditions during the events. Then the ENA observations are presented together with auroral images from the far-ultraviolet (FUV) imager onboard IMAGE. We then proceed by quantifying the timing of the dynamics in the ENA images. Geosynchronous observations of the magnetic field signatures from GOES and particle injection signatures from the Los Alamos National Laboratory (LANL) satellites are then put in relation to the signatures seen in the ENA images. Last we present and discuss the ion distributions derived from the ENA images through a constrained linear inversion technique. These observations show that the plasma sheet flux drops in association with dipolarization in about 30 min, but are quickly restored in the same time scale.

2. Observations

[8] In this section we will present the ENA images of the substorms, the energetic particle injections and dipolarizations seen at geosynchronous, and the auroral onset seen by IMAGE/FUV.

2.1. Storm Conditions

[9] The IMF B_z obtained from the ACE spacecraft is plotted together with the D_{st} index in Figure 1. The IMF data has been lagged by the solar wind velocity for the arrival at Earth. The 4 October 2000 storm displayed an almost 24 hour long mainphase due to a steadily decreasing IMF B_z. The thick line is the IMF-B_z and the thinner is the D_{st}. The two vertical lines at 06:10 UT and 09:22 UT mark the auroral onsets of the two substorms as defined by the far ultra violet (FUV) imager on board IMAGE.

2.2. Geosynchronous Ion Observations

[10] Figure 2 shows the 75-113 keV protons detected by the LANL satellite 1989-046. The vertical lines mark the

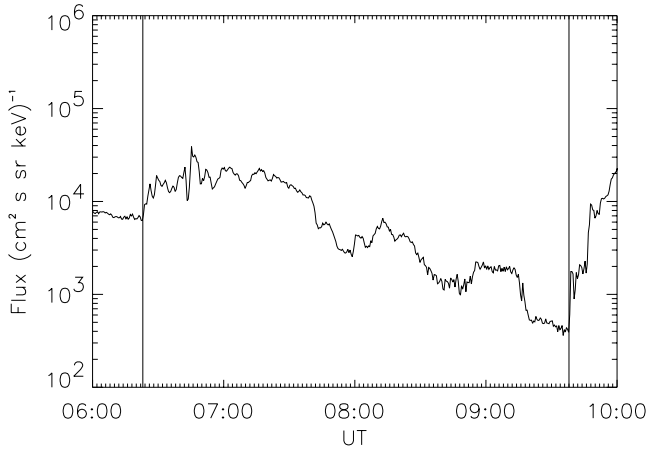

Figure 2. Plot of the 75-113 keV protons at geosynchronous. Vertical lines indicate the injections at 06:23 UT (19:23 MLT) and 09:38 UT (22:38 MLT).

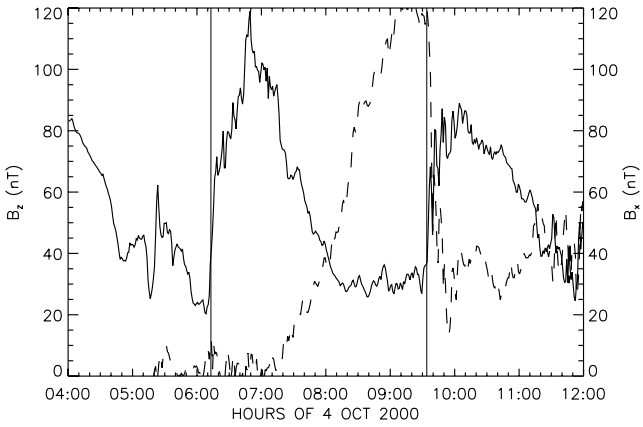

Figure 3. The B_x (dashed) and B_z (solid) component of the geomagnetic field at geosynchronous measured by GOES. The vertical lines mark the dipolarization signatures at 06:11 UT (21:22 MLT) and 09:34 UT (00:47 MLT).

injections detected at 06:23 UT (19:23 MLT) and 09:38 UT (22:38 MLT).

[11] Figure 3 shows the geomagnetic B_z (solid) and B_x (dashed) component in Geocentric Solar Magnetic (GSM) coordinates from the GOES satellite. The vertical lines mark the dipolarization signature associated with each substorm at 06:11 UT (21:22 MLT) and 09:34 UT (00:47 MLT). The first dipolarization shows very little change in the B_x component which could due to the fact that the GOES satellite was duskward of the stretched current sheet. At 07:00 UT the B_x component started to increase indicating a more stretched field configuration. At 09:34 UT we see the classical signature of the dipolarization with sharply decreasing B_x and increasing B_z.

2.3. ENA Observations

[12] Figures 4 and 5 show four ENA images during each substorm sequence for 10–60 keV and integrated over 6 min (3 spins). The ENA images are presented in an azimuthal equidistant projection with a 180° field of view (FOV). To illustrate the projection one can think of the detector being located in the center of a sphere, with the pole of the sphere being the direction of the spin axis. The image has then been wrapped onto the surface of this sphere and then back projected, with distances preserved, to the image plane tangential to the imagined sphere. The dashed gridlines in the background mark the latitude (horizontal lines) and the longitude (vertical lines) of this sphere. The latitude corresponds to the elevation angle in

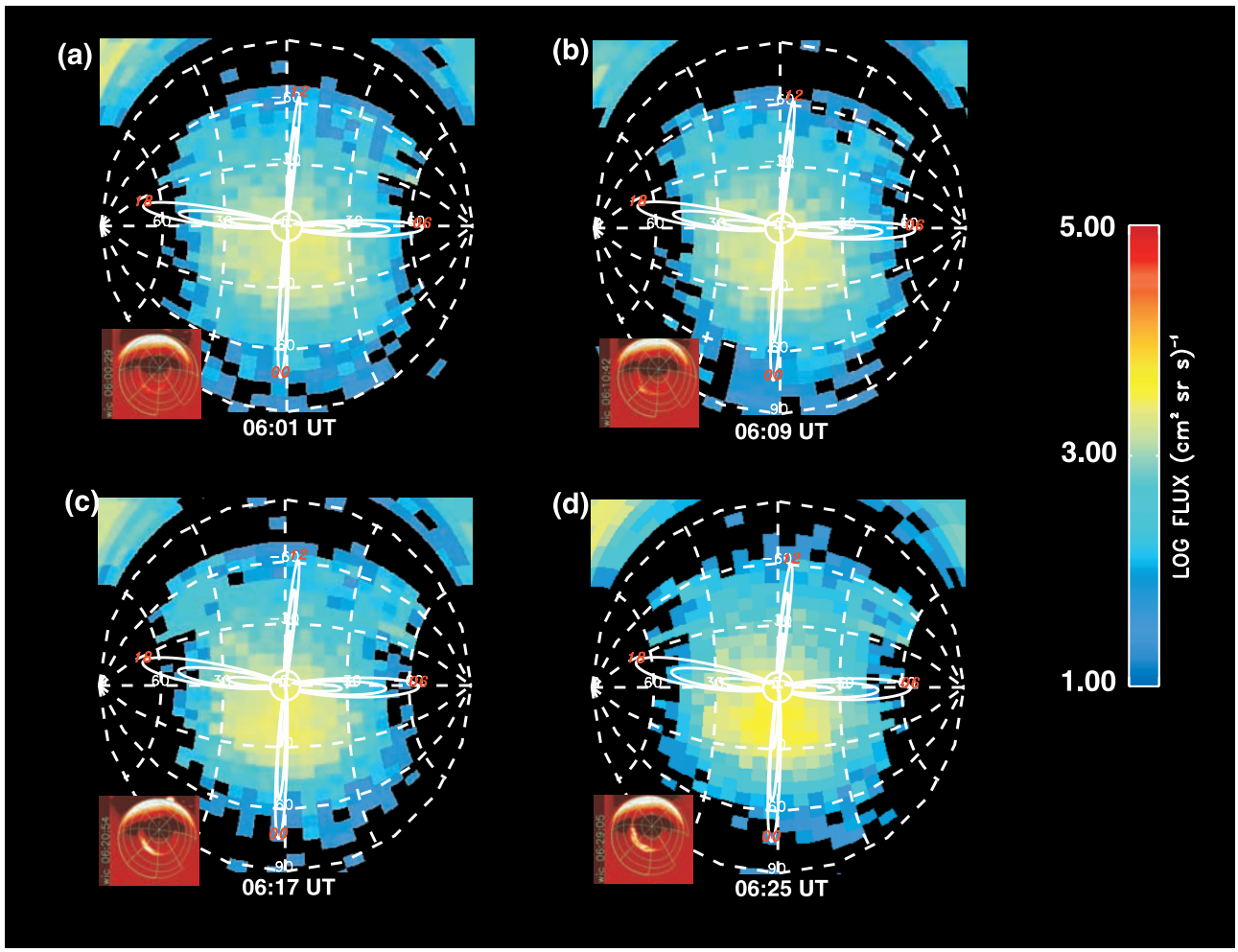

Figure 4. (a–d) The ENA images in the 10–60 keV range of the first substorm sequence with auroral onset at 06:10 UT. The inset is the auroral image obtained by the FUV/WIC camera on board IMAGE.

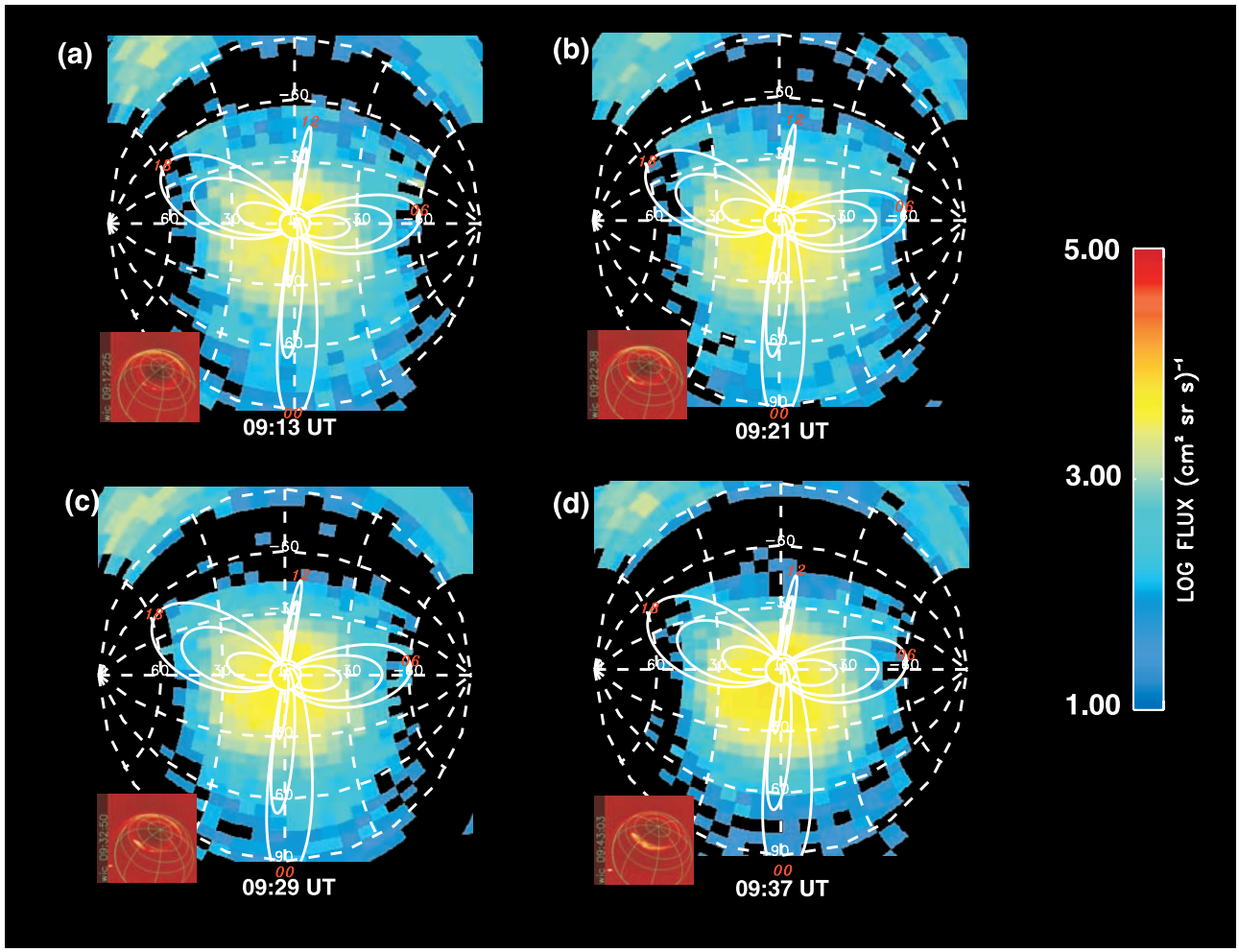

Figure 5. (a–d) The ENA images in the 10–60 keV range of the second substorm sequence with auroral onset at 09:22 UT. The inset is the auroral image obtained by the FUV/WIC camera on board IMAGE.

the instrument and the longitude corresponds to the spin angle. The coordinate system is geocentric. The circle about the center represents the limb of the Earth, while the arc inside the limb represents the terminator. The magnetic dipole field lines of L shells 4, 8 and 12 are drawn for reference at noon, dawn, midnight, and dusk. The magnetic local time (MLT) of each set of field lines is marked in red. All images are taken from a vantage point in the northern hemisphere. This projection type was chosen to accommodate a large range of different FOVs with maintained coverage. For FOVs less than 180° this projection comes close to what a human eye would see. However, for larger FOVs pixels at the edges will become distorted. The weak horizontal bands of emissions at the upper portions of each image (grid longitude −30°) are the solar contamination caused by residual sunlight hitting the detector plates.

[13] During the first sequence of images in Figure 4 we see how the nightside ENA flux increases with time in the $L \leq 4$ region. Note how the ENA emissions from the $L > 8$ region decrease with time. The auroral onset was determined from the IMAGE/FUV images to be at 06:10 UT, corresponding to Figure 4b. The substorm sequence with its onset at 09:22 UT had a clearer ENA signature and is shown in Figure 5. In this sequence it is more evident that the ENA fluxes in the $L > 8$ region decreased significantly after 09:32 UT.

[14] Below we will invert the isotropic component of the equatorial ion distribution from the ENA images in Figures 4 and 5. However, it would require an impractically large number of inversions to accurately time the dynamics.

[15] Therefore, we summed the region as marked in Figure 6a and plotted the summed intensities as a function of time. The summed region lies between −30° and +30° map latitude (instrumental elevational angle marked by the horizontal gridlines), and between 60° to 90° instrumental azimuth, which is marked by the vertical gridlines in Figure 6a and starts at nadir. In Figure 6b we have illustrated the approximate geometry in relation to the magnetospheric field. The dashed lines are the dipole field lines of L = 4, 6, 8, 10, and 12. The solid lines are the magnetic field lines from the Tsyganenko-96 (T96) magnetic field model [*Tsyganenko and Stern*, 1996]. A solar wind pressure of 2 nPa, *Dst* = −20 nT, and an IMF $B_x = B_y = B_z = 0$ nT were used. The corresponding McIlwain L-values for the T96 have not yet been calculated, but the main point of the illustration is to show that the sampled ENA emissions (the box in Figure 6a)

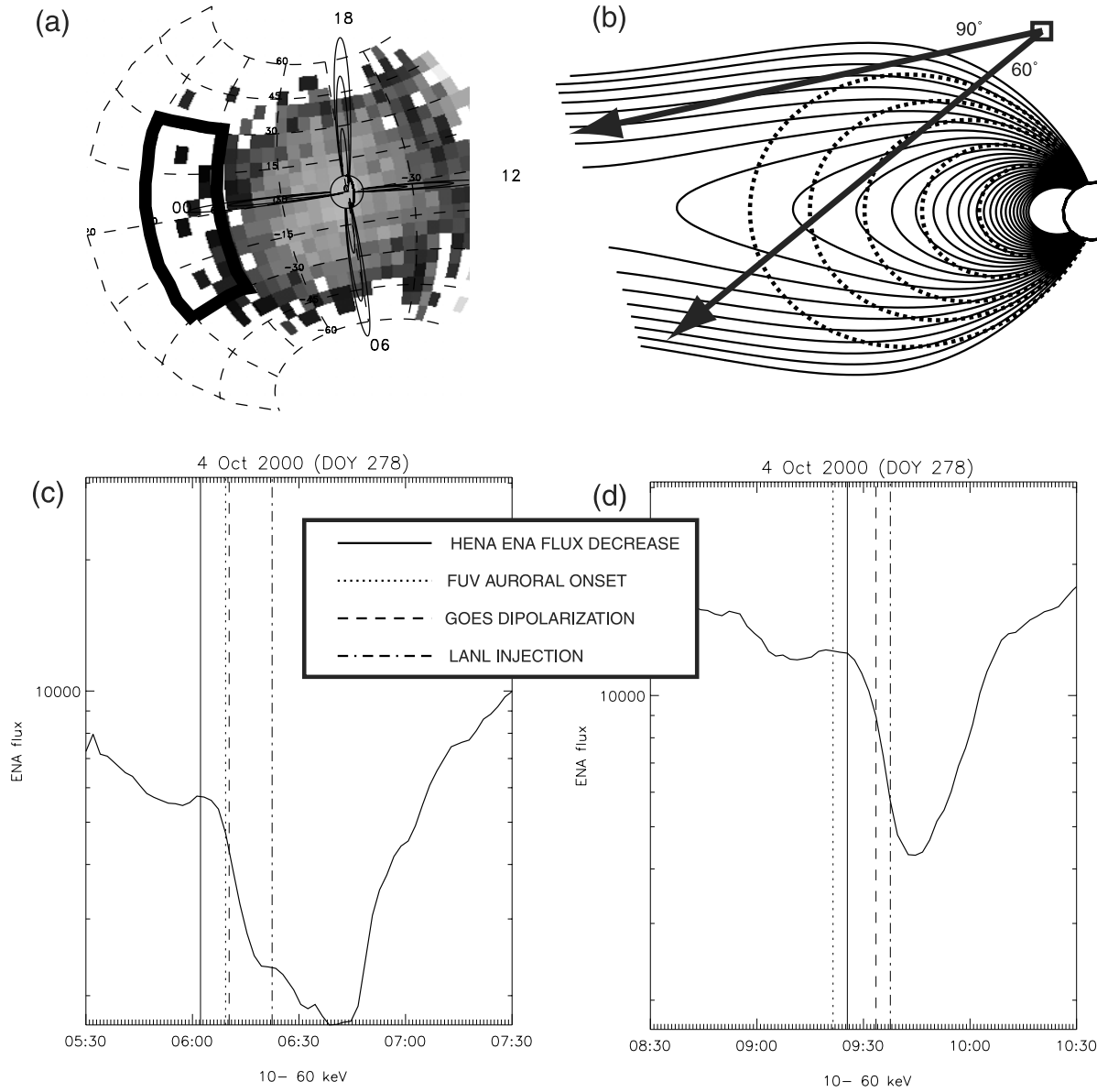

Figure 6. (a) In order to accurately time the dynamics the ENA emissions within the solid line are summed and plotted as a function of time in Figures 6c and 6d. (b) The viewing geometry in relation to the magnetic field. Dipole field lines (dashed) for L = 4, 6, 8, 10, and 12. More realistic field lines from the Tsyganenko-96 model (solid). (c) The total ENA intensity as a function of time for the 06:10 UT substorm. (d) The total ENA intensity as a function of time for the 09:22 UT substorm.

do not have any contributions from the inner magnetosphere. Developments are being made to more accurately incorporate a realistic magnetic field model into the analysis.

[16] These plots are shown for the two different substorms in Figures 6c and 6d. In Figure 6c we see how the ENA flux starts decreasing rapidly at 06:03 UT ±2 min. For this vantage point, the LOS which has its closest approach to the Earth for the sampled region, is the one that has its closest approach at L = 18 and 52° latitude. The radial distance at this point is about 6.7 R_E. The distance at the equatorial crossing is about 11 R_E. In both Figures 6c and 6d the dotted line marks the auroral onset identified by FUV; the dashed line marks when GOES observed the dipolarization; the dashed-dotted line marks when the particle injection reached the LANL satellite at geosynchronous. There is a corresponding rapid decrease for the around 09:26 UT ±2 min as can be seen in Figure 6d. Note that the auroral onset was about 4 min before the decrease of the L $\geq$ 10 ENA emissions here. For this vantage point, the LOS which has its closest approach to the Earth for the sampled region, is the one that has its closest approach at L = 8.4 and 25 latitude. The radial distance at this point is about 6.8 R_E. The distance at the equatorial crossing is about 7.6 R_E.

[17] If we assume that the sudden decrease in ENA flux seen in Figures 6c and 6d is due to an earthward motion of an isotropic plasma sheet ion distribution, we can do an interesting exercise. Let us use the proton injection times

observed by the LANL satellites and the plots in Figures 6c and 6d to estimate the speed of such an earthward motion. The question to ask is then: From what radial distance does the bulk ENA emissions that cause the drops in Figures 6c and 6d come from? Since ENA flux in general increases with decreasing altitude (because of the strong altitude profile of the hydrogen geocorona), the immediate response would be that they come from the LOSs that have the closest approach to Earth. However, if we take a look at the closest approaches of the LOSs of the sampled region they are 6.7 and 6.8 R_E for the two substorms, which give us an unreasonably low propagation velocity to geosynchronous (6.6 R_E). Let us instead take as representative distance the radial distance of the intersection of the closest approach LOS with the equatorial plane, which is 11 and 7.6 R_E for the two substorms. For the first substorm (06:10 UT) it was 20 min between the observed drop in ENA flux from the plasma sheet, and for the second it was about 12 min. Using the equatorial distances we then get propagation velocities of 24 and 5 km/s. These values are physically more reasonable and the reason for that may be that the LOSs go through a rather thin plasma sheet region where most of the ions are confined close to the equator. An upper bound can be estimated by assuming that the location of the ion distribution that contributed most to the drop in ENA flux in Figures 6c and 6d is at the edge of how far down the tail HENA can observe, which is approximately 14 R_E in equatorial crossing of the LOSs. The upper bound on the propagation then becomes 66 km/s. These values are consistent with the values average plasma flow velocities calculated by *Huang and Frank* [1994] and with convective flow velocities.

2.4. FUV Observations

[18] The auroral FUV observations are shown as insets in the lower left corner of Figures 4 and 5. The gridlines represent the geomagnetic latitude and longitudes. Latitude gridlines are 10° apart starting at the pole and longitude gridlines are 45° apart. The bright side of the globe is the dayside resulting from resonantly scattered sunlight. Note that the grid appears to change position from image to image. This is due to a wobble of the spacecraft spin axis during this particular date. One should not try to estimate any surface coordinates of the emissions from the grid. We can therefore not determine the magnetic latitude of the onset region. We have determined the two onset times from a high-resolution image sequence to 06:10 UT and 09:22 UT.

3. Inversion Method and Results

[19] The numerical method we use is called constrained linear inversion and closely follows the method described by *Twomey* [1977]. However, we utilize two new and essential features. First, the unknown variables to be inverted are simply the equatorial ion intensities $j_{ION}(L, \phi, \mu)$ at each discrete location $(L, \phi)_k$ bin in the magnetic equatorial plane. In other words, the output of the inversion method gives the ion distribution itself, rather than coefficients of its expansion in orthogonal functions or numerical splines [e.g., *Perez et al.*, 2001]. Not only does this direct formulation allow an immediate assessment of the physical appropriateness of the result, but it also allows a wider range of phenomenological patterns such as isolated injections and the plasma sheet to be reproduced. It is difficult to find a reasonable analytical representation that spans the same width in reproducibility. Second, the constraints of the inversion are determined by a novel "tuning" technique based on the ENA image itself. The inversion must be constrained, because the unconstrained problem is very poorly conditioned, i.e., the information in the data cannot uniquely determine some areas of the (L, ϕ) space.

[20] The number of counts accumulated in the ith camera pixel is written in terms of the averaged normal area $\langle A_i(\epsilon, \beta)\rangle$ of the camera seen by an ENA incident on the instrument from elevation angle ϵ and azimuth angle β.

$$C_i = \Delta t \int d\epsilon \sin\epsilon \int d\beta \langle A_i(\epsilon,\beta)\rangle J_{ENA}(\epsilon,\beta) \qquad (1)$$

[21] We write $J_{ENA}(\epsilon, \beta)$ for $j_{ENA}(\epsilon, \beta)\Delta E$ because we assume that the energy (or velocity) pass bands ΔE are narrow enough so that there is no significant variation in the camera response. The integral over the angles (ϵ, β) in principle covers the entire sky (4π sr) and not just the small solid angle of a single pixel. This is because each pixel has a "point-spread" function owing to internal scattering that can be significantly larger than the pixel itself. The averaging of A_i is over the time Δt during which the counts are accumulated in the pixel, e.g., a minimum of one spin (Δt = 120s) for IMAGE/HENA. It also must be integrated over the solid angle of the pixel and any significant orbital motion of the spacecraft during the exposure time for the pixel. All properties of the ENA camera must be incorporated into the function $\langle A_i(\epsilon, \beta)\rangle$. Examples for other ENA instruments have been published: the MEPI particle telescope on ISEE-1 [*Roelof*, 1987] and the PIPPI camera on Astrid-1 [*C:son Brandt et al.*, 2001].

[22] The well-known relationship between the differential number flux j_{ENA} and j_{ION} for an "ENA optically thin" medium is expressed in terms of a line-of-sight (LOS) integral. The simplest case is that of "high-altitude" ENA imaging of ring current ions immersed in the hydrogen geocorona

$$j_{ENA} = \sigma_H^{1,0}(E) \int ds n_H(r) j_{ION}^{eq}\left(L, \phi, \mu_{eq}\right), \qquad (2)$$

where **s** is the distance vector from the point of emission **r** the camera at position **R** along the LOS. Thus **s** = **R** − **r** gives the direction of the ENA. The cross section for charge exchange is $\sigma_H^{1,0}(E)$, and $n_H(r)$ is the geocoronal hydrogen density. We assume that there is negligibly weak scattering of the ion along the magnetic field line. Then the magnetic moment $(1 - \mu^2)/B$ is conserved and the ion intensity jion with pitch-cosine μ at any point on a field line may be related via Liouville's theorem to j_{ION}^{eq} with pitch-cosine μ_{eq} at that lines' equatorial crossing. Again, we shall assume energy resolution good enough that j_{ENA} and j_{ION}^{eq} may be replaced by $J_{ENA} = j_{ENA}\Delta E$ and $J_{ION}^{eq} = j_{ION}^{eq}\ \Delta E$.

[23] Now equations (1) and (2) may be combined. Usually, the integrations are carried out as indicated, first along

the LOS and then over the angular response of the instrument. However, the triple integral over the instrument arrival solid angle and LOS can be transformed into a volume integral in geomagnetic spherical polar coordinates. The exact Jacobian is r^2/s^2, so we have

$$d\epsilon \sin\epsilon d\beta ds = dr d\theta \sin\theta d\phi \frac{r^2}{s^2}, \tag{3}$$

where θ is the geomagnetic co-latitude and ϕ is the magnetic longitude (MLT). If we furthermore approximate the geomagnetic field by a dipole, then $dr = (\arcsin^2\theta)dL$ when the innermost integral over volume is taken over θ. Obviously, $a = 1\ R_E$. The final result is

$$C_i = \int dL \int d\phi K_i(L,\phi) J^{eq}_{ION}\left(L,\phi,\mu_{eq}\right), \tag{4}$$

where

$$K_i(L,\phi) = a\sigma^{1,0}_H \Delta t \int d\theta \sin^3\theta \frac{r^2}{s}\, n_H(r)\langle A_i(\epsilon,\beta)\rangle \tag{5}$$

[24] In passing from equation (4) to (5) we have neglected the pitch-angle dependence in J^{eq}_{ION} (L, ϕ, μ_{eq}), i.e., we have made the approximation of an isotropic equatorial ion distribution. This will be adequate for this paper, which only deals with ENA images taken at high latitudes during periods when pitch-angle effects appear to be negligible.

[25] The integral over colatitude θ for the kernel in equation (5) is carried out (using an efficient integration algorithm) for each equatorial position bin $(L, \phi)_k$. Then the double integral in equation (4) can be approximated by linear quadratures.

$$C_i = \Sigma_k K_i(L,\phi)_k J^{eq}_{ION}(L,\phi)_k \Delta L \Delta\phi, \tag{6}$$

where the index k runs over all equatorial position bins (L, ϕ). We have thus achieved our goal of formulating an ENA image inversion explicitly in terms of the equatorial ion intensities indexed by their position bins $(L, \varphi)_k$.

[26] In more concise matrix/vector notation we write $\mathbf{C} = \mathbf{KJ}$, where $\mathbf{K}$ is a non-square matrix because there are more pixels (i) than position bins (k). The elements in $\mathbf{K}$ are not exactly $K_i(L, \phi)_k$, but rather are linear combinations thereof resulting from the particular quadrature formula applied to equation (4). A constrained least-squares solution for this linear system is *Twomey* [1977]

$$\mathbf{J} = (\mathbf{KTK} + \gamma\mathbf{H})^{-1}\mathbf{K}^T\sigma^{-2}\mathbf{C} \tag{7}$$

where σ^{-2} is the inverse of the covariance matrix of the pixel counts, $\mathbf{H}$ is a smoothing matrix, and γ is the constraint strength.

[27] Now we come to the second innovation, the "tuning" of the constraint strength. The "regularization" $\gamma\mathbf{H}$ must be large enough to stabilize the inversion, but small enough to avoid unnecessary distortion. In nearly all cases that we have tested, the unconstrained inversion ($\gamma = 0$) is very poorly conditioned. In order to "tune" the regularization, we first simulate an ENA image using equation (4) with the 38-parameter model developed by *Roelof and Skinner* [2000]. We choose the parameters to produce a test ion distribution $J^{(0)}_k$ that we estimate should produce an ENA image similar to the one we are trying to invert. This could be thought of as a first guess at the result. We add Poisson counting statistics to the counts $C^{(0)}_i$ in the simulated ENA image. We then invert the image using equation (7) and our first guess at the value of the constraint strength $\gamma^{(0)}$. This gives us a solution $J^{(1)}_k$ that we compare with $J^{(0)}_k$. This comparison tells us if $\gamma^{(0)}$ was too small (inversion ill-conditioned) or too large (solution overly smoothed), leading us to our next guess $\gamma^{(1)}$. We can also adjust the form of $\mathbf{H}$ at each step. We have tried several forms of $\mathbf{H}$ and have found that the minimum length solution ($\mathbf{H} = \mathbf{I}$, the identity matrix) consistently exhibits the most stable behavior. We repeat this process n times until we find a suitable combination of $\gamma^{(n)}$ and $\mathbf{H}^{(n)}$, i.e., one such that $\mathbf{J}^{(n)}_k$ reproduces the essential spatial features of the test distribution $J^{(0)}_k$. Finally, we obtain our actual solution by using $\gamma^{(n)}$ and $\mathbf{H}^{(n)}$ in equation (7) to invert the observed pixel counts C_i for our best estimate of the equatorial ion intensities $J(L, \phi)_k$.

[28] In brief, what we have done is to iteratively "tune" the regularization so that it faithfully retrieves a test ion distribution that can simulate an ENA image that looks like the observed ENA image. If the test intensity function is similar to the actual ion intensity that we finally invert from the ENA image, then our process is consistent. This "tuning" process is greatly facilitated by formulating the inversion problem directly in terms of the equatorial ion intensity distribution $J^{eq}_{ION}(L, \phi, \mu_{eq})$ as specified in equation (4).

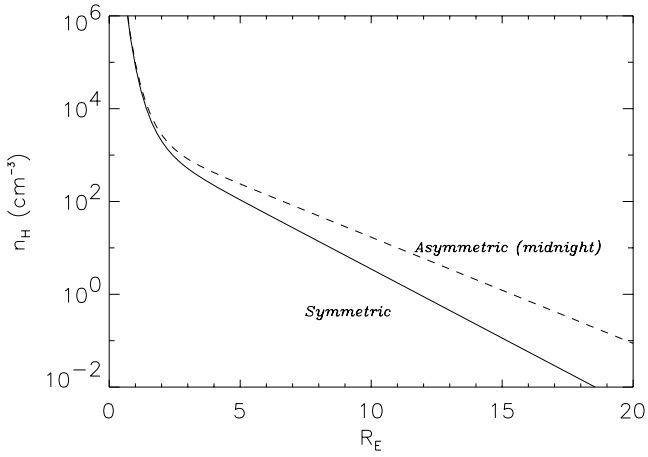

Figure 7. The two exospheric models used. The dashed line display enhanced exospheric densities at large altitudes on the nightside.

4. Exosphere

[29] To illustrate the effects of the exosphere we use here the symmetric Chamberlain model [*Chamberlain*, 1963] and an asymmetric model based on the DE-1 measurements reported by *Rairden et al.* [1986]. They provided measured column densities of the nightside exosphere which showed

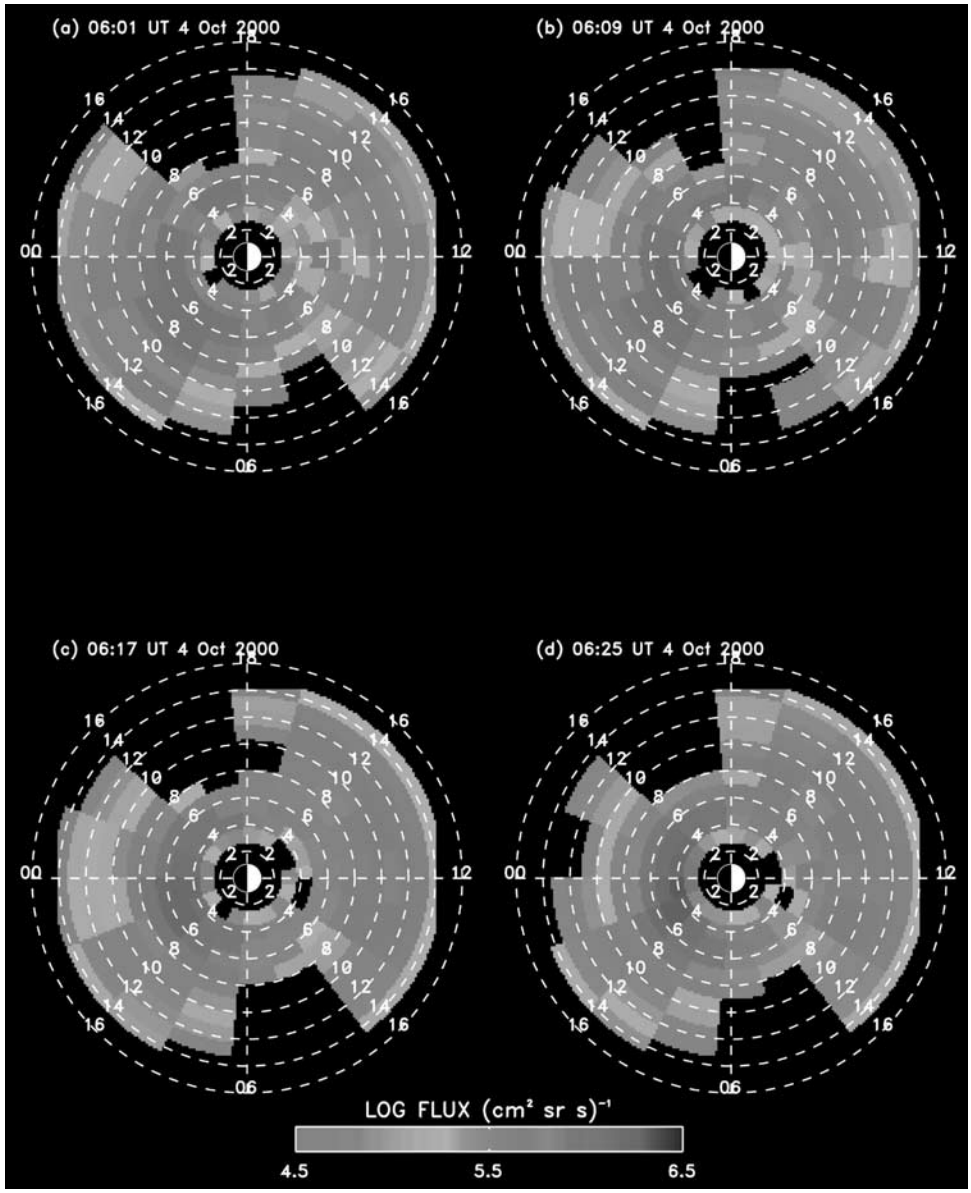

Figure 8. T (a–d) The inverted ion distributions in the 10–60 keV range (6 min integration) for the 06:11 UT substorm using the symmetric *Rairden et al.* [1986] model exosphere (see equations (8) and (9)).

an excess over the symmetric Chamberlain model which often is referred to as a "geotail." Both models can be described by

$$n(R,\phi) = 3300 \exp\left[17.5e^{-1.5R} - \frac{R}{H(\phi)}\right], \quad (8)$$

where

$$H(\phi) = 1.46[1 - k\sin(\theta)\cos(\phi)]. \quad (9)$$

Here ϕ is the local time angle from noon and θ is the polar angle from the z-axis in the Geocentric Solar Magnetic (GSM) coordinate system. A non zero value of k allows one to represent the geotail in the form of an axis-symmetric (around the Sun-Earth line) exosphere. Setting $k = 0$ restores the symmetric Chamberlain model. All numeric coefficients in the above expressions have been obtained from the fit to the Chamberlain model by *Rairden et al.* [1986]. By fitting their column densities of the geotail to equations exo1 and exo2 we obtain $k = 0.3$. The symmetric and axis-symmetric model is plotted for $\phi = 180$ in Figure 7. We would like to stress that although the existence of a geotail is confirmed, the quantitative knowledge is thin.

5. Results

[30] The ENA images in Figures 4 and 5 have been inverted using the two exospheric models above ($k = 0$ and $k = 0.3$ in equation (9)).

[31] The inversions of the ENA image sequence in Figure 4 are shown in Figures 8 with the symmetric exosphere and in Figure 9 with the asymmetric exosphere. The

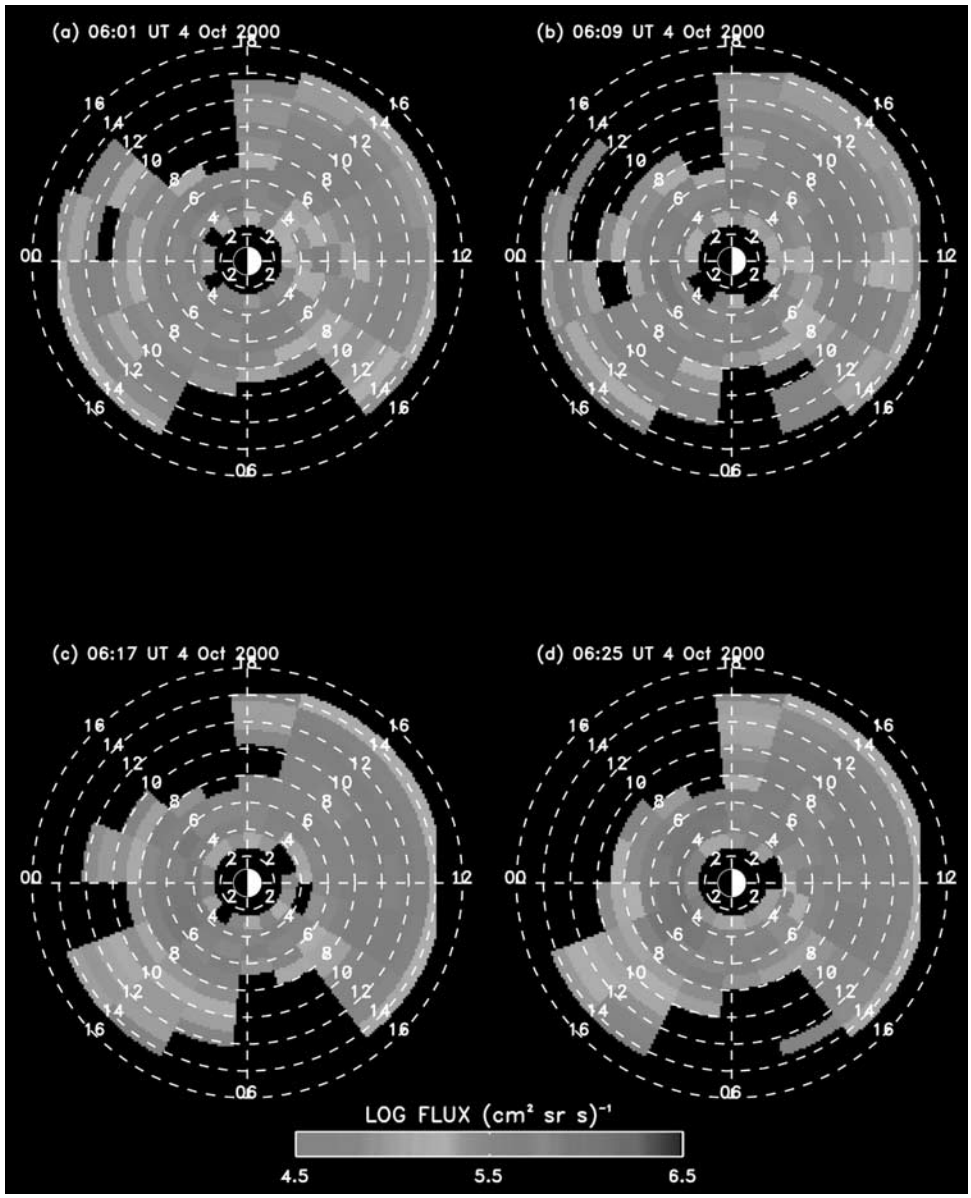

Figure 9. (a–d) The inverted ion distributions in the 10–60 keV range (6 min integration) for the 06:11 UT substorm using the asymmetric *Rairden et al.* [1986] model exosphere with $k = 0.3$ from equations (8) and (9).

ion distribution is plotted in L-MLT coordinates out to L = 15. In fact, the ion flux in the inversion is clamped to zero at L < 2 and L > 15.

[32] The effects from the contamination of residual sunlight in the detector is clearly visible on the dayside at L > 6 as the enhanced intensities. We have chosen to show the contamination in this paper to illustrate how and when it effects the data, and more important, how to eliminate it from the ion distribution. The LOSs toward the Sun contamination in Figures 4 and 5 (above map grid longitude −30°) intersects a minimum L-shell of 6 for both substorms and therefore ion distributions below L = 6 are free of solar contamination. Also, the field of view (FOV) of the instrument cuts off the edges outside |45°| instrumental latitude. Here the sensitivity of the instrument is low and thus the response function amplifies the uncertainties. Therefore we stress that the empty regions on the dusk and dawn sides in the inverted results below are the effects of the finite FOV of the instrument and not zero flux.

[33] At 06:01 UT (Figure 8a) the ion distribution display large fluxes out to 13 R_E in the post midnight sector with its peak at 6 R_E. The enhancement around 6 R_E extends from post midnight to the dusk sector. In the remaining sequence (Figures 8b–8d) the nightside fluxes above 7R_E decreases. The peak of the ion distribution moves earthward from about 6 R_E to 5 R_E and spreads also in local time.

[34] Figure 9 shows the sequence of inversions using the asymmetric exospheric model with $k = 0.3$. It is immediately clear that the ion fluxes are in general weaker than for the inversions in Figure 8 with $k = 0$. The reason for this is that the asymmetric exosphere displays higher density than the symmetric model does, as can be seen

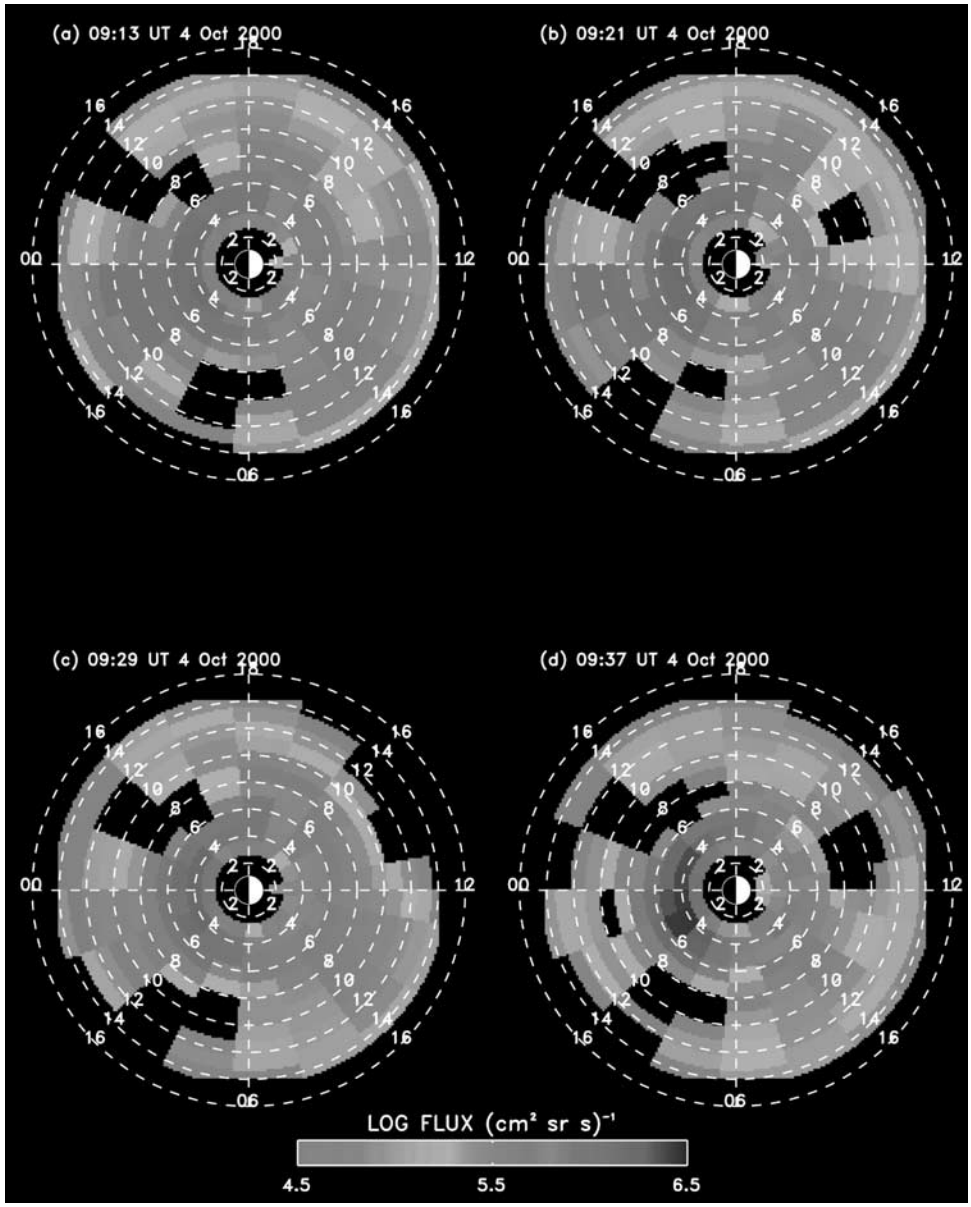

Figure 10. (a–d) The inverted ion distributions in the 10–60 keV range (6 min integration) for the 09:22 UT substorm using the *Rairden et al.* [1986] model exosphere (see equations (8) and (9)).

in Figure 7 and so less ion flux is required to match the observed ENA images. At 06:01 UT there are relatively high ion fluxes out to 13 R_E, which move gradually earthward throughout Figures 9b–9d. We can see that the peak ion flux moves from 6 R_E to about 4 R_E and expand also in local time.

[35] A similar development can be seen for the 09:22 UT substorm shown in Figures 10 and 11. The corresponding ENA images are shown in Figure 5. Figure 10 shows the inversion using the symmetric model exosphere with $k = 0$. The overall fluxes are slightly higher than for Figure 8 and appears to be more confined in MLT. Again, we see intense ion fluxes out to 13 R_E that decreases throughout the sequence that may be interpreted as an earthward motion. The peak ion flux moves from 5 R_E to 4 R_E as it also increases due to the substorm injection. Figure 11 shows the inversion using the asymmetric model exosphere with k = 0.3. Again, the overall fluxes are lower than the symmetric model.

[36] In Figure 10a a minimum appears to develop in the 2230–0130 MLT wedge at around 7 R_E. One may be tempted also to attribute a tailward propagation of this minimum, or the maximum beyond it. Although interesting we must caution the reader that this could be an effect of our use of a pure dipole field in the inversion. Any findings concerning this feature will be reported in a future paper.

[37] The use of a realistic magnetic field model in the inversion is essential to be able to correctly interpret the results. We are currently working on integrating a stretched magnetic field model into the inversion, and the basic question will always be how the inversion results are effected by different stretched magnetic topologies. In this paper we take the opportunity to explore the extreme case of

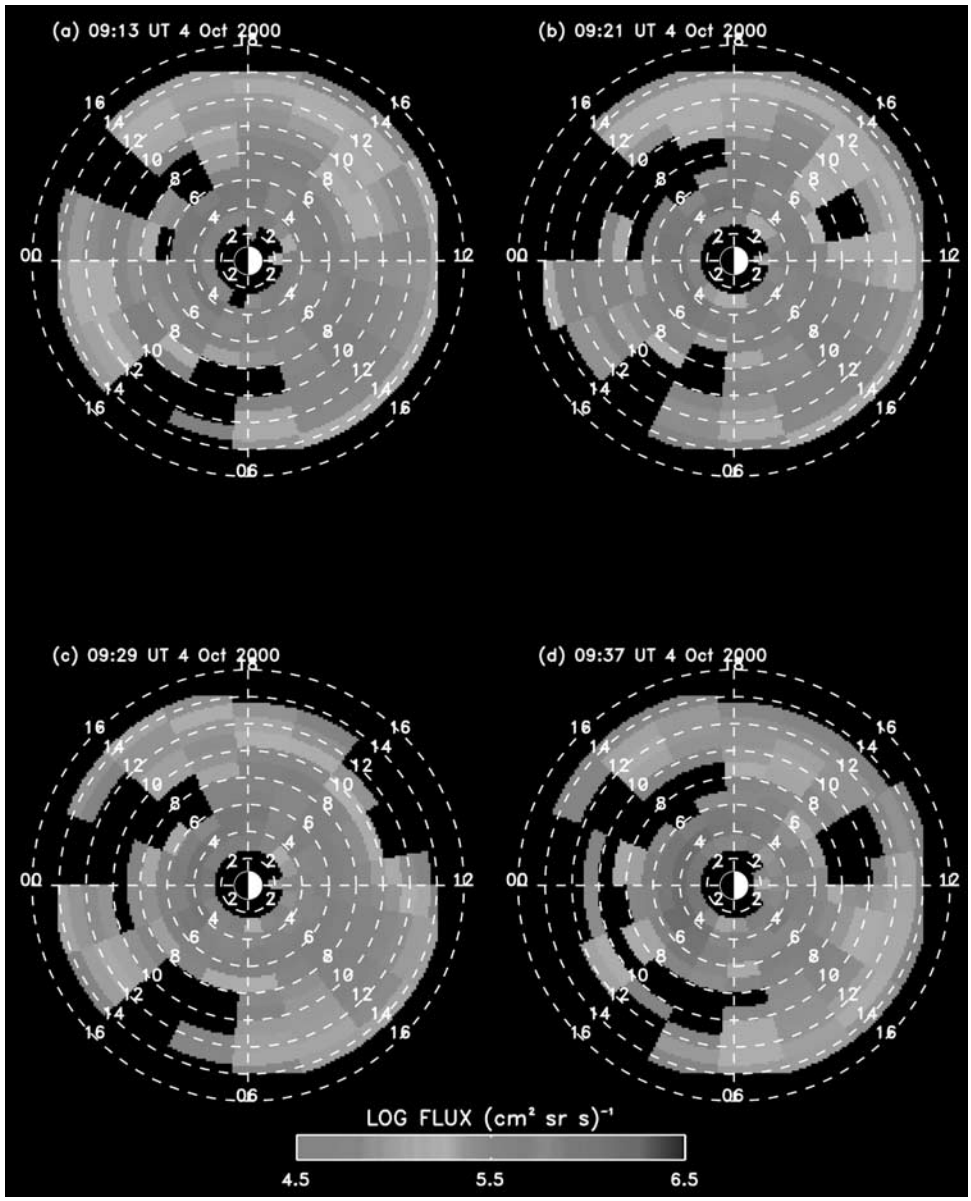

Figure 11. (a–d) The inverted ion distributions in the 10–60 keV range (6 min integration) for the 09:22 UT substorm using the asymmetric *Rairden et al.* [1986] model exosphere with $k = 0.3$ from equations (8) and (9).

using a dipole field. Let us consider the outermost edge of the ENA emissions and its relation to magnetic field configuration.

[38] Figure 12a shows the ENA image from 09:13 UT and the cross marks the LOS towards the outermost edge. Our question is where the ENA emissions in this LOS come from. Figure 12b shows the midnight-noon meridional plane where we have taken a couple of field lines from the T96 model (solid) and overplotted dipole field lines (dashed) for dipole L-values 4, 6, 8, 10, and 12. The LOS corresponding to the direction marked in Figure 12a is shown. Any other LOS outside the emission region (with larger azimuthal angles in this case), will not contain any counts. The inversion will interpret this as emission only coming from the region bound by L-shell with which the outermost LOS is tangent to (the bold L-shell). The LOSs towards the ''edges'' for the vantage points analyzed in this paper have their equatorial crossings at around 20 R_E and higher. In this region the stretching is so significant that the ion distributions are confined to low latitudes in the plasma sheet, such as illustrated by the shaded area in Figure 12b. Therefore the ENA emissions from the outermost LOSs have come from a region as far out as 20 R_E or more. Thus, the use of a dipole field in the inversion puts a lower bound on the radial location of the ion distribution.

6. Discussion

[39] It is worthwhile attempting to put our observations in a physical context. Here we outline a plausible scenario. Before substorm onset at 06:10 UT the cross tail electric

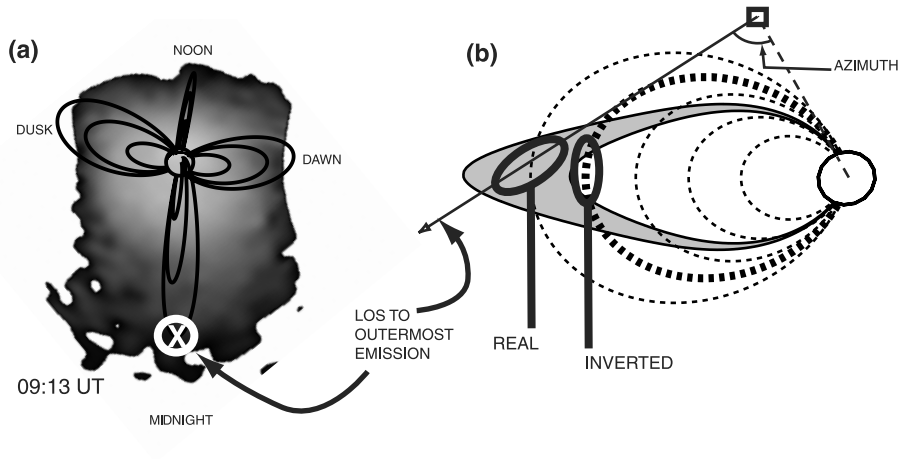

Figure 12. Sketch illustrating the effect of using a dipole magnetic field model in the inversion. (a) An ENA image from 09:13 UT showing the location of the outermost edge of the emission region. The white cross marks the selected LOS direction. (b) Solid lines represent the stretched field configuration and the dashed lines represent the dipole field lines of L = 4, 8, 10, and 12. The radial location of the outer edge retrieved from the inversion will be underestimated if a dipole field model is used.

field appears to be enhanced due to a negative or very small positive IMF B_z. This enhances the convection from the dayside magnetopause and the earthward $\mathbf{E} \times \mathbf{B}$ drift on the nightside, resulting in a tail and a plasma sheet with higher ion flux than normal. This appears as the higher ion flux above geosynchronous altitude in Figure 8. The IMF B_z steadily decreases and therefore the cross tail current will build up until it disrupts at some place due to some internal instability [*Lui*, 1991] or triggering from the NENL [*Baker et al.*, 1996; *Ohtani*, 2001; *Slavin et al.*, 2002]. The disruption causes the stretched magnetic field configuration to dipolarize which induces an intense dawn-to-dusk electric field pulse. The dipolarization is observed at geosynchronous by GOES around 06:11 UT as shown in Figure 3. At this time the ion fluxes at geosynchronous have increased slightly. The reason for the rapidly decreasing plasma sheet flux accompanying the dipolarization, is that the induced dawn-to-dusk electric field will transport the ions earthward through enhanced E × B drift, faster than the particles can be replenished by the overall $\mathbf{E} \times \mathbf{B}$ drift set up by the convectional electric field. This mechanism was also suggested by [*Lui*, 1991]. The ions have now reached lower altitudes and have been energized through betatron and possibly fermi acceleration. This is where they are observed by the LANL satellite in Figure 2.

[40] Now, since the IMF B_z is still decreasing to more negative values, a steady supply of plasma is convected in from the dayside over the poles on reconnected field lines and will increase the nightside ion flux as soon as the first dipolarization and the substorm injection is complete. The plasma sheet will thin, the cross tail current will build up and the process will repeat itself for the next substorm. This pattern repeated itself several times during the entire day of 4 October.

[41] Our inversion technique only contains a static dipole field and yet we know that the magnetic field stretches and dipolarizes. The remaining question is therefore, how does the thinning of the plasma sheet and the dipolarization effect the ENA fluxes? During the thinning of the plasma sheet the PADs probably maintain their isotropy and so the ENA flux should decrease since the thickness of the source region decreases. *C:son Brandt et al.* [2002] reported a decrease of the ENA fluxes between 08:00 UT and 09:09 UT decrease during the substorm growth phase during the 4 October 2000 storm. They attributed other effects as well to the decrease.

[42] During dipolarization the z-component of the magnetic field increases abruptly which implies that plasma sheet thickens. The PADs of protons during the dipolarization are expected to remain isotropic at large. Once the ion distributions are transported by the substorm electric field to lower L-shells their perpendicular energy is expected to increase due to the conservation of their magnetic moment. Since the protons during the field reconfiguration are not expected to change their PAD, the sudden decrease of ENA flux from the plasma sheet, as seen in Figures 6c and 6d, and Figures 4 and 5, is most likely due to an earthward propagation of the ion distribution in the plasma sheet.

[43] From our observations it appears that the particle pressure increased in the 6–14 R_E plasma sheet in the recovery phases of the two substorms (except for the period 08:00–09:09 UT [*C:son Brandt et al.* 2002]). At dipolarization the pressure outside 8 R_E decreased rapidly while the pressure inside 8 R_E increased. *Kistler et al.* [1992] found that the pressure increased at distances <10 R_E and either decreased or stayed the same outside 10 R_E over the substorm. We feel that it may be dangerous to generalize the pressure profiles of substorms without studying the IMF. The reason is that an enhanced external cross tail electric field enhances the earthward $\mathbf{E} \times \mathbf{B}$ drift and therefore increases the particle pressure through adiabatic energization. However, the loading of fresh solar wind plasma from the lobes would act to decrease the temperature of the plasma sheet and therefore act as a competing process to cool the plasma sheet. This balance between these processes are clearly dependent on IMF and a deeper study of their effect is beyond the scope of

this paper. Several facts imply that the ions do undergo an earthward propagation: (1) After plasma sheet fluxes decrease, the fluxes around geosynchronous increase; (2) Several studies of in-situ measurements have shown that earthward flow precedes the substorm onset and occurs within 30 R_E [*Nagai et al.*, 1998; *Ohtani*, 2001].

7. Summary and Conclusions

[44] We have presented the first global images and ion distributions of the Terrestrial plasma sheet out to at least 14 R_E. The images were obtained by the HENA instrument on board IMAGE during two substorms in the mainphase of the 4 October, 2001, storm. A constrained linear inversion method was used to derive the proton distribution from the ENA images. The inversion uses a dipole magnetic field and an exospheric model based on the DE-1 observations reported by *Rairden et al.* [1986]. The use of a dipole model was found to underestimate the radial location of the ion distributions retrieved from the inversion. We summarize our findings as follows.

1. Before the substorm the ion fluxes above geosynchronous were high due to an enhanced convection in the storm mainphase.

2. ENA fluxes beyond 8 R_E started to decrease 12–20 min before geosynchronous proton injection was detected by the LANL satellites. If we assume that the plasma sheet ion distributions were isotropic throughout the substorm, we can use the time of the first observed decrease of ENA fluxes from the plasma sheet to the time of detection of the geosynchronous injection to put an upper bound of 66 km/s on the earthward propagation velocity.

3. The decrease of ENA fluxes from the plasma sheet can be interpreted as the plasma sheet ions being accelerated earthward by the induced substorm electric fields faster than they can be replenished from the overall convection. After the substorm, plasma sheet ion fluxes increase due to the refilling from the convection.

4. The use of a symmetric exospheric model based on the fit by *Rairden et al.* [1986] gave peak plasma sheet fluxes at L = 10 about $5 \cdot 10^5$(cm sr s)$^{-1}$, while an asymmetric exosphere, with a nightside excess of neutral densities, gave about a factor of five lower plasma sheet flux.

[45] If our scenario behind the ENA flux decrease from the plasma sheet is correct, it would imply that the onset of the earthward flows must be localized to at least the region where we see the plasma sheet fluxes decrease during dipolarization. If the onset of earthward flow was simultaneous and throughout the tail region we would not see a decrease of fluxes in the plasma sheet, but rather an increase.

[46] **Acknowledgments.** Lou-Chuang Lee and Chin S. Lin thank Michael G. Henderson and J. A. Slavin for their assistance in evaluating this paper.

References

Baker, D. N., T. I. Pulkkinen, V. Angelopoulos, and W. Baumjohann, Neutral line model of substorms: Past results and present view, *J. Geophys. Res.*, *101*, 12,975–13,010, 1996.

Burch, J. L., ed., *The IMAGE Mission*, Kluwer Acad., Norwell, Mass., 2000.

Chamberlain, J. W., Planetary coronae and atmospheric evaporation, *Planet. Space Sci.*, *11*, 901–960, 1963.

C:son Brandt, P., S. Barabash, E. C. Roelof, and C. J. Chase, ENA imaging at low altitudes from the Swedish microsatellite Astrid: Extraction of the equatorial ion distribution, *J. Geophys. Res.*, *106*, 25,731–25,744, 2001.

C:son Brandt, P., S. Ohtani, D. G. Mitchell, M. C. Fok, E. C. Roelof, and R. Demajistre, Global ena observations of the storm mainphase ring current: Implications for skewed electric fields in the inner magnetosphere, *Geophys. Res. Lett*, doi:10.1029/2002GL015160, in press, 2002.

Huang, C. Y., and L. A. Frank, A statistical survey of the central plasma sheet, *J. Geophys. Res.*, *99*, 83–95, 1994.

Kistler, L. M., E. Möbius, W. Baumjohann, G. Paschmann, and D. C. Hamilton, Pressure changes in the plasma sheet during substorm injections, *J. Geophys. Res.*, *97*, 2973–2983, 1992.

Lui, A. T. Y., A synthesis of magnetospheric substorm models, *J. Geophys. Res.*, *96*, 1849–1856, 1991.

Mitchell, D. G., et al., High energy neutral atom (HENA) imager for the IMAGE mission, *Space Sci. Rev.*, *91*, 67–112, 2000.

Nagai, T., et al., Structure and dynamics of magnetic reconnection for substorm onsets with geotail observations, *J. Geophys. Res.*, *103*, 4419–4440, 1998.

Ohtani, S.-I., Substorm trigger processes in the magnetotail: Recent observations and outstanding issues, *Space Sci. Rev.*, *95*, 347–359, 2001.

Ohtani, S., S. Kokubun, and C. T. Russell, Radial expansion of the tail current disruption during substorms: A new apporach to the substorm onset region, *J. Geophys. Res.*, *97*, 3129–3136, 1992.

Perez, J. D., G. Kozlowski, P. C. Brandt, D. G. Mitchell, J. M. Jahn, C. J. Pollock, and X. Zhang, Initial ion equatorial pitch angle distributions from energetic netural atom images obtained by IMAGE, *Geophys. Res. Lett.*, *28*, 1155–1158, 2001.

Rairden, R. L., L. A. Frank, and J. D. Craven, Geocoronal imaging with dynamics explorer, *J. Geophys. Res.*, *91*, 13,613–13,630, 1986.

Reeves, G. D., M. G. Henderson, P. S. McLachlan, R. D. Belian, R. H. W. Friedel, and A. Korth, Radial propagation of substorm injections, in Third International Conference on Substorms, *Eur. Space Agency Spec. Publ.*, *ESP-389*, 579, 1996.

Roelof, E. C., Energetic neutral atom image of a storm-time ring current, *Geophys. Res. Lett.*, *14*, 652–655, 1987.

Roelof, E. C., and A. J. Skinner, Extraction of ion distributions from magnetospheric ENA and EUV images, *Space Sci. Rev.*, *91*, 437–459, 2000.

Slavin, J. A., et al., Simultaneous observations of earthward flow bursts and plasmoid ejection during magnetospheric substorms, *J. Geophys. Res.*, *107*(A7), doi:10.1029/2000JA003501, 2002.

Tsyganenko, N. A., and D. P. Stern, Modeling the global magnetic field of the large-scale Birkeland current systems, *J. Geophys. Res.*, *101*, 27,187–27,198, 1996.

Twomey, S., *Introduction to the Mathematics in Remote Sensing and Indirect Measurements, Develop. Geomath.*, vol. 3, 1st ed., Elsevier Sci., New York, 1977.

P. C:son Brandt, R. Demajistre, D. G. Mitchell, S. Ohtani, and E. C. Roelof, Applied Physics Laboratory, Johns Hopkins University, Laurel, MD 20723-6099, USA. (pontus.brandt@jhuapl.edu)

S. Mende, Space Science Laboratory, University of California, Centennial Dr. at Grizzly Peak Blvd., Berkeley, CA 94720-7450, USA.